Hard X-Ray Flares and Spectral Variability in NGC 4395 ULX1

Tanuman Ghosh[1] , Vikram Rana[1] , and Matteo Bachetti[2]
[1] Astronomy and Astrophysics, Raman Research Institute, C.V. Raman Avenue, Sadashivanagar, Bangalore 560080, India; tanuman@rri.res.in
[2] Istituto Nazionale di Astrofisica-Osservatorio Astronomico di Cagliari, via della Scienza 5, I-09047 Selargius (CA), Italy

Abstract

We report the detection of flaring events in NGC 4395 ULX1, a nearby ultraluminous X-ray source (ULX), for the first time, using recent XMM-Newton observations. The flaring episodes are spectrally harder than the steady-emission intervals, resulting in higher fractional variability in the high-energy regime. A thin Keplerian and a slim accretion disk provide the best-fit continuum for XMM-Newton spectra. All observations show a broad hump-like feature around ~ 0.9 keV, which can be associated with a collection of blended emission lines, and suggests the presence of a wind or outflow in this ULX through comparison with other ULXs that show a similar feature. The flaring spectra correspond to higher slim-disk temperatures due to a higher mass accretion rate under an advection-dominated accretion scenario. The luminosity–temperature (*L-T*) values in different flux states show a positive trend. When characterized with a power-law relation, the *L-T* profile is broadly consistent with both $L \propto T^2$ and $L \propto T^4$ relations for the analyzed data. The empirical predictions for a slim accretion disk in the case of super-Eddington accretion onto a stellar-mass compact object is $L \propto T^2$, which is a possible scenario in ULX1. The origin of the flaring events is understood as an intrinsic change in accretion rate or presence of variable clumpy wind in the inner region of the accretion disk.

Unified Astronomy Thesaurus concepts: Ultraluminous x-ray sources (2164); X-ray binary stars (1811)

1. Introduction

Ultraluminous X-ray sources are the brightest off-nuclear X-ray binaries, having emission luminosities above the Eddington limit of a 10 $M_\odot$ black hole ($L_x > 10^{39}$ erg s^{-1}; see Kaaret et al. 2017 for a recent review). Compared to the sub-Eddington Galactic X-ray binaries (XRBs) or active galactic nuclei (AGNs), ULXs show distinct spectral curvature below 10 keV (see, e.g., Bachetti et al. 2013; Walton et al. 2013, 2014, 2015a, 2015b; Rana et al. 2015; Mukherjee et al. 2015; Fürst et al. 2017), suggesting that these sources are mostly super-Eddington stellar-mass compact object accretors. Indeed, a number of ULXs were found to have neutron star accretors, confirming this super-Eddington interpretation (Bachetti et al. 2014; Fürst et al. 2016; Israel et al. 2017a, 2017b; Brightman et al. 2018; Wilson-Hodge et al. 2018; Vasilopoulos et al. 2020; Chandra et al. 2020; Carpano et al. 2018; Rodríguez Castillo et al. 2020; Sathyaprakash et al. 2019).

ULX spectra show two common features—a characteristic turnover below 10 keV and a soft excess ⩽1 keV. These properties are typically explained by disk wind emission in the scenario of super-Eddington accretion (Shakura & Sunyaev 1973; Poutanen et al. 2007). The mass outflow rate and the viewing angle of the disk determine the spectral softness, with softer sources being observed nearer to the plane of the disk (see Middleton et al. 2015a; Pinto et al. 2021 and references therein). Strong blueshifted atomic features are one of the signature characteristics of such relativistic ($\beta \sim 0.25$) wind emission (Pinto et al. 2016, 2017, 2020; Kosec et al. 2018a, 2018b; Walton et al. 2016; Middleton et al. 2015b), which can share a large fraction of the total energetic budget of ULXs.

ULXs are broadly categorized into four classes (Sutton et al. 2013; Kaaret et al. 2017). Broadened disk (BD) sources exhibit hot thermal spectra from a geometrically modified disk, related to the supercritical slim-disk scenario (Begelman 1979; Abramowicz et al. 1988, 1989). These sources belong to the lowest luminosity regime of ULXs (~ 1–3×10^{39} erg s^{-1}), and the typical accretion rate of these sources is near or slightly above the Eddington accretion rate. The higher luminosity ULXs mostly show two-component spectra in 0.3–10.0 keV energy range, a soft thermal component, and a hard component. Depending on the hardness of the sources, they are classified as hard ultraluminous (HUL) or soft ultraluminous (SUL) sources.

ULXs with a power-law index $\Gamma > 2$ in the 0.3–5.0 keV energy band are classified as SUL sources (Pinto et al. 2021). A subclass of these are supersoft ultraluminous (SSUL) sources or ultraluminous supersoft sources (ULSs), which have most of their observed flux at energies below ~ 1 keV. The bolometric luminosity of these sources is typically a few 10^{39} erg s^{-1}, and their spectra are mostly dominated by a cool blackbody component ($T_{bb} < 0.14$ keV; Urquhart & Soria 2016; Pinto et al. 2021). However, some sources, such as NGC 55 ULX and NGC 247 ULX-1, are considered to be soft ULX sources but fall somewhere between ULX and ULS spectral states (see Figure 1 of Pinto et al. 2017). Unlike most ULSs, they show spectra that extend up to ~ 5 keV, and typically, their spectra are best modeled by two blackbody components (Pinto et al. 2017, 2020, 2021).

Modern X-ray instruments have observed a large number of ULXs. However, only a few sources have shown short-term timing variability in terms of fractional variability and quasiperiodic or periodic oscillation. A number of sources such as NGC 1313 X1 (Walton et al. 2020), NGC 7456 ULX-1 (Pintore et al. 2020), NGC 253 ULX-1 (Barnard 2010), NGC 6946 ULX-3 (Earnshaw et al. 2019), NGC 247 ULX-1 (Pinto et al. 2021), 4XMM J111816.0-324910 in NGC 3621 (Motta et al. 2020), NGC 4559 X7 (Pintore et al. 2021), and M82 X-1
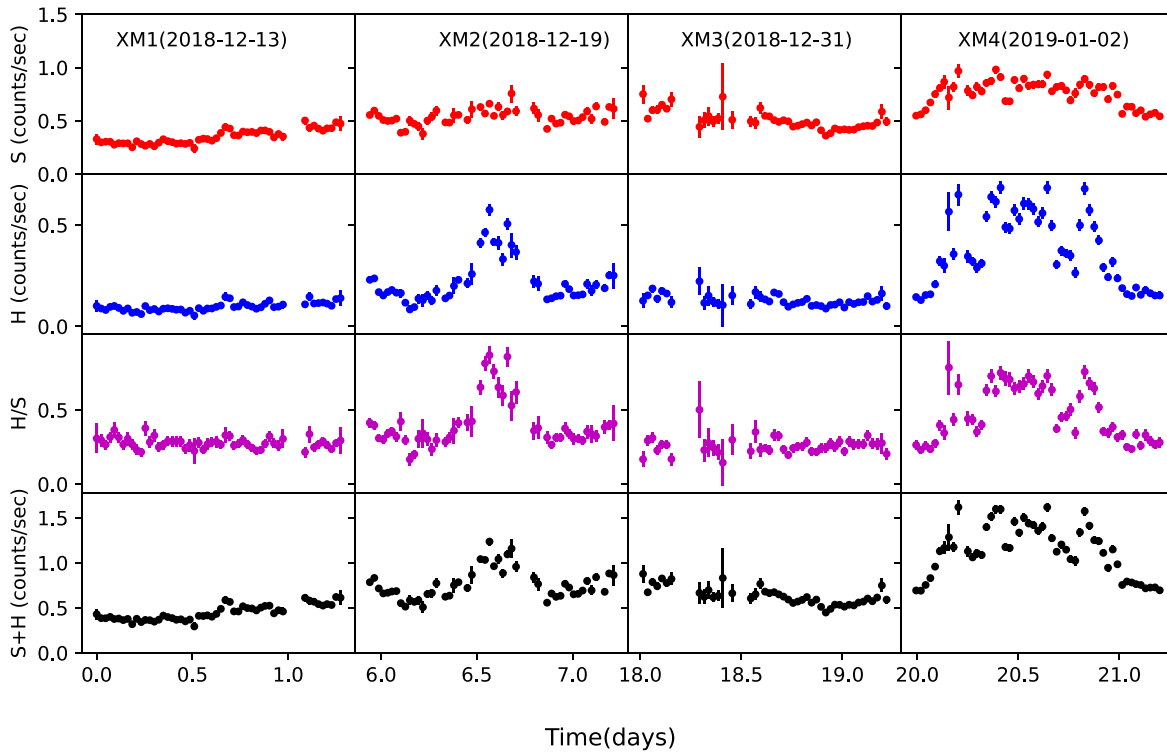
Figure 1. XMM-Newton pn light curves of ULX1 for four individual epochs binned by 2000 s. The first panel shows the soft (0.3–1.0 keV) count rate, the second panel shows the hard (1.0–8.0 keV) count rate, the third panel shows the hardness ratio defined as hard/soft photon count rate, and the fourth panel shows the sum of the soft- and hard-band light curve, i.e., the total light curve. The first epoch (XM1) shows a steady but slight uprising trend of the flux, the second epoch (XM2) shows a flaring episode that occurred from around 30 to 80 ks of that observation, the third epoch (XM3) shows another steady but slightly declining trend of flux, and the fourth epoch (XM4) finally shows a large flaring episode that covered most (~80 ks) of that observation. The prominent flares in XM2 and XM4 are predominant in the hard band, as seen in the hardness ratio plots.

Table 1
Observation Log of NGC 4395 ULX1

Serial No.	Observation ID	Date of Obs.	Epoch ID	Cleaned Exposure (ks) pn/MOS1/MOS2
1	0824610101	2018-12-13	XM1	71/89/94
2	0824610201	2018-12-19	XM2	48/67/69
3	0824610301	2018-12-31	XM3	50/66/70
4	0824610401	2019-1-2	XM4	77/97/100

Note. The exposure times noted here are flare-corrected approximate live-time CCD exposures.

(Brightman et al. 2016) have been found to show some intermittent flaring events. These flaring activities can help shed light on the dynamics of accretion processes or wind outflows in these sources.

NGC 4395 ULX1 (2XMM J122601.4+333131; Liu & Bregman 2005) is a ULX that has shown long-term variability (Kaaret & Feng 2009). Vinokurov et al. (2018) suggested that the source might exhibit a period of 62.8 days in archival observations. Earnshaw & Roberts (2017) studied this source using previous XMM-Newton and Chandra observations. These data showed no significant short-term timing variability in this source. In this paper, we present a detailed study of four high-quality XMM-Newton observations, two of which show flaring activities from this source for the first time.

2. Data Analysis

XMM-Newton (Jansen et al. 2001) observed the NGC 4395 galaxy four times between 2018 December and 2019 January to study the AGN (Pi McHardy). ULX1 is around ~3′ away from the galaxy's active nucleus. In the XMM-Newton EPIC detectors, ULX1 is well isolated from any other X-ray sources. The details of the observation log are given in Table 1. The four observations studied here are abbreviated as XM1 (0824610101), XM2 (0824610201), XM3 (0824610301), and XM4 (0824610401) for ease of reference in the rest of the paper.

Using the standard data reduction procedure of the XMM-Newton data analysis software SAS v19.1.0,[3] we clean the data from soft-proton and background flaring events and extract the science products for all EPIC-pn and MOS1/2 instruments. We select source photons from a circle of 25″ radius centered at α, $\delta = 12:26:01.5, +33:31:31.0$ and background photons from a circle of 50″ radius in a nearby source-free region on the same chip.

---
[3] https://www.cosmos.esa.int/web/xmm-newton/sas

Unfortunately, ULX1 falls near the chip gap in all pn data. Additionally, the pn data are affected by strong bad column events in the source region in all observations. XM3 and XM4 data are mostly affected because a significant fraction of the source region falls in the chip gap, and the bad column passes through the central region of the source. This causes flux loss in pn spectra due to substantial charge loss. XM1 and XM2 pn data are comparatively less affected because the bad column passes through the edge of the source. We have performed spectral analysis of individual pn and MOS1/2 data for all epochs and found that the chip gap and bad column issue in pn observations do not affect the spectral profile, except for a flux loss in XM3 and XM4 observations (see Section 4 for details). Hence, for the subsequent spectral analysis, pn and MOS1/2 data are fitted simultaneously for each observation with different spectral models.

The fast timing analysis is done on minimally filtered data in order to maximize the number of counts and to be sensitive to short-time variability. However, for the spectral analysis, we set a strict constraint of FLAG $==0$ to extract pn spectra for all observations to minimize the charge-loss effect in the data. Spectra are grouped using SPECGROUP with a grouping factor of 20 counts per energy bin at least and an oversampling factor 3 for using χ^2 statistics. Light curves are extracted using EVSELECT for single and double events in pn (PATTERN $<=4$), and single, double, triple, and quadruple events in MOS (PATTERN $<=12$). The background-corrected source light curves are generated using the EPICLC-CORR task, which corrects vignetting, bad pixels, chip gaps, point-spread function (PSF), and quantum efficiency. For the timing analysis, we have performed barycentric correction on the events using the barycen tool of SAS. Pileup in the data is evaluated with EPATPLOT, and no significant pileup is found.

We have also analyzed RGS data following standard data extraction procedures. However, the RGS spectra of the source are dominated by the background in all four observations. The combined RGS1+RGS2 spectral count rate (in full energy range) varies between ~0.007 and 0.016 counts s^{-1} in different epochs, whereas the cleaned exposure varies between ~171 and 226 ks.

3. Timing Analysis

Previous X-ray observations portrayed NGC 4395 ULX1 as the least variable source in the sample of soft ULXs studied in Earnshaw & Roberts (2017). However, the XMM-Newton observations analyzed here show both short-term (on a timescale of a few kiloseconds) and long-term (on a timescale of a few days) timing variability.

The 2000 s binned XMM-Newton pn light curves for all epochs are shown in Figure 1. From a visual inspection, it appears that while in XM1 and XM3, the source has a relatively steady flux, in XM2 and XM4, it shows flare-like activity. In order to check any energy-dependent nature of the flaring behavior, we divide the time series into two energy bands. We set the soft band between 0.3 and 1 keV (Figure 1 first panel), and the hard band is above 1 keV (second panel). Although the background starts to dominate above ~5 keV for XM1 and XM3 epochs and ~8 keV for XM2 and XM4 epochs (see Section 4.1), to make a direct comparison of all four epochs, we create the light curves in the hard band between 1.0 and 8.0 keV for all four epochs. The hardness ratio in the third

panel of Figure 1 is defined as the ratio of the hard photon count rate to the soft photon count rate. The fourth panel of the figure shows the sum of the soft- and hard-band light curves. The figure shows how the ULX1 count rate varies between different epochs within a three-week period. The XM2 observation shows a significant short-term flaring incident lasting ~50 ks, mostly prominent in the hard energy band. The longest flaring episode is detected during the XM4 observation, where the flaring lasted for ~80 ks, a large portion of the observing span. The long flare of the XM4 epoch consists of multiple ephemeral subflaring episodes. However, the minimum count rate level of these transient subflares is much higher than the persistent count rate level of the XM1 and XM3 epochs. So, we consider the whole ~80 ks long flare in XM4 as a single flaring epoch for our analysis. As there are no flaring events in XM1 and XM3, the hardness ratio is nearly constant for these two epochs. On the other hand, for XM2 and XM4, the hardness ratio demonstrates that the variability in different energy bands is prominent, and the flaring events are more significant in the harder spectral band (above ~1 keV).

Studying the short-term variability is essential to decipher the inherent properties of transient events that occur in ULXs. The first task to find this variability is to perform a Fourier space investigation of the time series. The power spectral density (PSD) analysis provides no evidence of quasiperiodic or periodic oscillations in any of the observations, except for the presence of red noise at low frequencies in a few cases. We also search for transient pulsation in the time series. We incorporate the acceleration search technique to detect any transient pulse while correcting the Doppler shift due to binary orbital period correction. Tools such as HENDRICS (Bachetti 2018) and PRESTO (Ransom 2011) are employed for these tasks. We use the EPIC-pn data for this purpose because this telescope has the highest time resolution of ~73.4 ms. We use the HENACCELSEARCH task of HENDRICS to search for pulsation in the 0.3–8.0 keV energy range and in the frequency range of 0.01–6.8 Hz to avoid artifacts due to the Nyquist limit. We use a maximum number of Fourier frequency bins (z_{max}) of 100 with a Fourier frequency bin resolution (Δz) of 1. No significant pulsation is detected in any epoch. We also search for pulsation in the same energy and frequency ranges using HENzsearch, with a fast-folding algorithm that searches for the first spin derivative. Here also, no pulsation is found in any observation. However, this tool estimates an upper limit on the pulsed amplitude $\frac{I_{max} - I_{min}}{I_{max} + I_{min}}$ for the best candidate frequency within 90% confidence, where I_{max} and I_{min} are the maximum and minimum values of the folded profile, respectively. We can estimate the upper limit on the pulsed fraction $\frac{I_{max} - I_{min}}{I_{max}}$ from this pulsed amplitude value. We find that the upper limit of the pulsed fraction varies between $\sim10\%$–17% in these four epochs. We further divide XM2 and XM4 observations into three subepochs (see the left and right panels of Figure 2, respectively): preflare, flare, and postflare intervals. Pre- and postflare intervals have similar count rates and overlapping spectral properties. Hence they are combined and referred to as a "nonflaring" interval. We perform a similar exercise to search for pulsation in these segmented flaring and nonflaring intervals using the aforementioned methods. No pulse period is found in either case. The upper limits of the pulsed fraction for these segmented intervals vary between $\sim11\%$–23%. We also use the accelsearch tool from the PRESTO package by invoking the jerk search
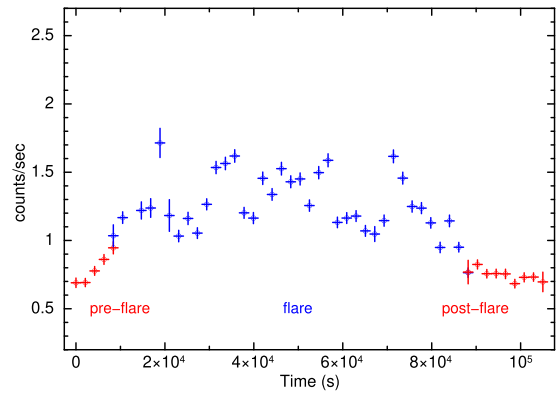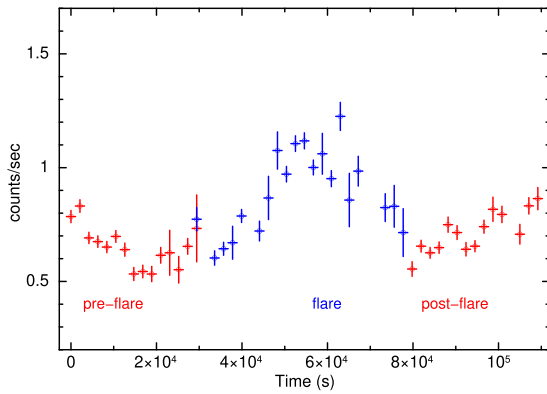
Figure 2. Different transient intervals are defined for the XM2 (left) and XM4 (right) epochs of observation. The preflare, flare, and postflare intervals are indicated separately. The preflare and postflare intervals are combined to obtain the nonflaring interval.

technique. Here, we use a maximum number of Fourier frequency bins of 200 and a maximum number of Fourier frequency derivative bins, $w\text{max} = 600$ (Andersen & Ransom 2018), within the same frequency range as before. Again, no significant pulsation is found.

The light curves of NGC 4395 ULX1 also demonstrate significant short-term variability in terms of the fractional root mean square (rms) variability amplitude (F_{var}), which measures the variance of a source over the Poissonian noise in the time series, normalized to the average count rate (Vaughan et al. 2003; Edelson et al. 2002). $F_{\text{var}} = \sqrt{\frac{S^2 - \bar{\sigma}^2}{\bar{x}^2}}$, where $S^2 = \frac{1}{N-1}\sum_{i=1}^{N}(x_i - \bar{x})^2$ and $\bar{\sigma}^2 = \frac{1}{N}\sum_{i=1}^{N}\sigma_i^2$. x_i is the count rate at ith bin, $\bar{x}$ is the mean count rate, N is the total number of bins, σ_i is the uncertainty in count rate in the ith bin. The error on F_{var} is measured as $\sigma_{F_{\text{var}}} = \frac{1}{F_{\text{var}}}\sqrt{\frac{1}{2N}}\frac{S^2}{\bar{x}^2}$. We use the soft and hard light curves of each XMM-Newton pn observation and bin them to 1000 s, then we estimate F_{var} and its error. The fractional variability values are listed in Table 2. We also use the MOS observations to verify whether the variability in pn light curves is an artifact of the bad column or chip gap, as described in Section 2. First we add MOS1 and MOS2 light curves to increase the count statistics (for both soft and hard energy bands) and bin the net light curves by 1000 s. We find that the same trend of variability is seen in both pn and MOS data (see table 2). Hence, we confirm that these variabilities are an intrinsic property of ULX1. This calculation clearly shows that fractional variability is higher in epochs XM2 and XM4 compared to epochs XM1 and XM3 above 1.0 keV.

4. Spectral Analysis

In this section, we report the spectral analysis results of the XMM-Newton observations in detail. We use XSPECv12.12.0 (Arnaud 1996) for the spectral analysis throughout the paper. The absorption is quantified using the Tuebingen-Boulder ISM absorption model (TBABS in XSPEC) for the Galactic and local extinction contributions. The updated abundance (Wilms et al. 2000) and photoionization cross-section (Verner et al. 1996) are used. The Galactic absorption column[4] is kept fixed to 0.04×10^{22} cm^{-2} (HI4PI Collaboration et al. 2016). The local absorption column is allowed to vary as a free parameter. Throughout the paper, the statistical uncertainties in the

Table 2
Fractional Variability in pn and MOS Light Curves for All Four Epochs

Epoch	pn		MOS	
	Soft	Hard	Soft	Hard
XM1	0.17 ± 0.02	0.17 ± 0.02	0.15 ± 0.02	0.11 ± 0.04
XM2	0.11 ± 0.01	0.52 ± 0.04	0.12 ± 0.02	0.47 ± 0.04
XM3	0.15 ± 0.02	0.08 ± 0.06	0.19 ± 0.02	0.09 ± 0.05
XM4	0.15 ± 0.01	0.47 ± 0.03	0.14 ± 0.01	0.47 ± 0.03

spectral parameters are within the 90% confidence interval unless mentioned otherwise.

4.1. Time-averaged Spectroscopy

We start by analyzing the spectra of individual observations. We plot MOS1 spectra for all epochs (top left panel) in Figure 3. XM1 and XM3 have similar spectra in terms of flux and spectral feature, and both of them exhibit steep spectra extending only up to 5 keV, after which background starts to dominate. XM2 and XM4 epochs have comparatively harder spectra and higher flux than the other two epochs and extend up to 8 keV, after which the signal-to-noise ratio (S/N) decreases significantly.

Because there is a chip gap and strong bad column issue in pn data, we perform an exercise to verify whether they affect the source spectral properties. First of all, we carry out an individual analysis of pn and MOS1/2 data for all observations with a simple absorbed power-law model and a Gaussian component (see details of the spectral models below) and find that the spectral parameters in the pn data are consistent with MOS1/2 data within the 90% statistical confidence interval, with the only exception of the normalization of the power law in XM3 and XM4. Therefore, in the following, we simultaneously fit pn and MOS1/2 data for each observation with a cross-calibration constant fixed to 1 for MOS1 and left free to vary in MOS2 and pn. All other parameters of the models used are tied between the instruments. These cross-calibration values are within 10% of MOS1, except for the pn data of the XM3 and XM4 epochs, which are most affected by the noisy detector column and chip gap, as described in Section 2.

To quantify the contribution of different emission mechanisms in ULX1 spectra, we fit them with various physical and phenomenological models in XSPEC. A simple power-law fit is useful to characterize the spectral hardness of the individual epochs. XM1 and XM3 epochs have a power-law index (Γ)
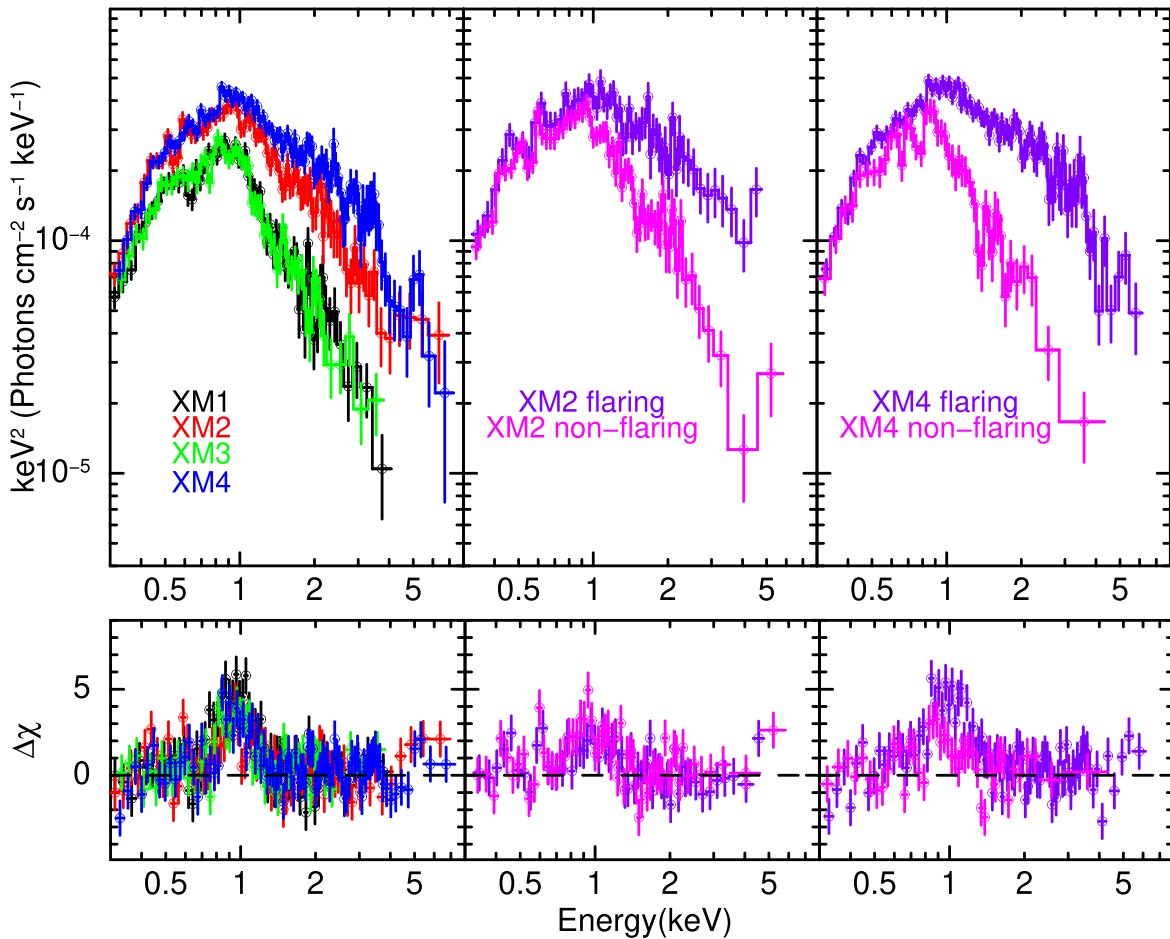

Figure 3. Top: unfolded MOS1 spectra for different epochs are plotted using the `powerlaw` model of the zero photon index ($\Gamma = 0$). For plotting purposes, the normalization of the model is kept arbitrarily high. ULX1 exhibits a significant long-term spectral variability in different observation epochs. The MOS1 spectra of the XM1 and XM3 epochs in the left panel show overlapping spectral features. The XM2 and XM4 epochs clearly show differences in spectral shapes and a divergence in the hard spectral regimes. Flaring and nonflaring spectra of the XM2 and XM4 epochs are plotted in the middle and right panels. These two figures have a similar divergence in spectral characteristics above 1 keV. Bottom: the residuals of the best-fit continuum are shown for MOS1 spectra corresponding to the epochs shown in the top panels. To show the significant contribution of the Gaussian in the spectra, for plotting purposes, the Gaussian component is removed from the best-fit model.

value of ~4.6 and ~4.8, respectively, whereas XM2 and XM4 epochs have ~3.7 and ~3.5, respectively. It is interesting to compare the photon indices found for NGC 4395 ULX1 with those seen from canonical black hole X-ray binaries, which can range from ~1.7 in the low/hard state to ~2.5 in the steep power-law state or in the very high state (Remillard & McClintock 2006). Thus, ULX1 has much steeper spectra in all four epochs compared to the sub-Eddington black hole X-ray binaries. Using this power-law continuum, a soft excess around ~0.4 keV and a Gaussian emission-like feature around ~0.9 keV are also detected. If we use a more complicated model composed of a thermal blackbody disk, a power law, and a Gaussian, we are able to fit the ULX1 spectra for all epochs. However, the power-law model extends to low energies arbitrarily, making the parameters of the power-law model degenerate with those of the low-energy components such as the extinction or the emission lines. Hence, we explore other models, seeking a physically consistent description of ULX1 spectra.

Many ULX spectra, from soft ULXs such as NGC 55 ULX and NGC 247 ULX-1 to moderately hard ULXs such as NGC 1313 X1 and NGC 4559 X7, have been modeled with the composition of models with two thermal components (Pinto et al. 2017, 2020; Kara et al. 2020; Walton et al. 2020;

Pintore et al. 2021). One thermal component describes the cooler accretion disk emission from the outer disk region, which is geometrically thin, and the other component describes the hot inner disk component, the geometry of which depends on the accretion rate of the system. Especially for ULXs, when the accretion rate becomes close to or above the critical accretion rate, the disk becomes an advection-dominated disk or a slim accretion disk. This physical scenario motivates us to explore a continuum that consists of a thin accretion disk and a slim accretion disk. For NGC 4395 ULX1, we find that one cool thin disk (DISKBB in XSPEC) plus a comparatively hotter slim accretion disk (DISKPBB in XSPEC, with $p = 0.50$) provide an adequate fit for the continuum at all epochs. We find that the parameter p of DISKPBB always assumes a value close to the lower limit of the parameter, 0.50, corresponding to a slim-disk regime. Hence we fix this p value to 0.50. In addition to the continuum, a broad Gaussian around 0.9 keV is always required. We find that before addition of the Gaussian component, the χ^2/dof for only continuum fits are 402/171 for XM1, 297/209 for XM2, 255/143 for XM3, and 375/241 for XM4 epochs. These fits are significantly improved after the addition of a Gaussian component (see Table 3). In XSPEC syntax, the best-fit model we use is `TBABS(GAL)*TBABS*(GAUSS +DISKBB+DISKPBB)`. The N_H value is consistent in all

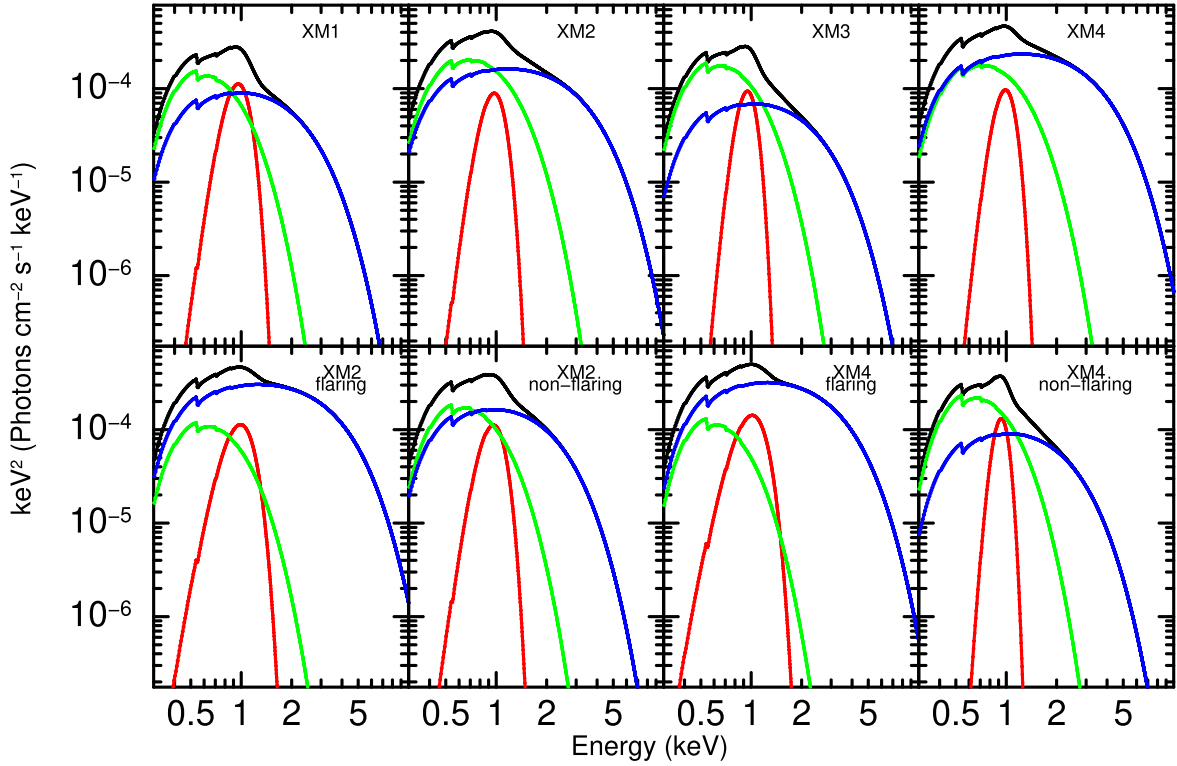**Figure 4.** The model components for MOS1 spectra for different epochs. The red component is the `GAUSSIAN`, green represents the `DISKBB`, and blue represents `DISKPBB` components. Black represents the total model. The variation in `DISKPBB` model due to flaring incidents is clear from the figure.

Table 3
Best-fit Model (`TBABS(GAL) * TBABS * (GAUSS+DISKBB+DISKPBB)`) Parameters of NGC 4395 ULX1 for the Four Epochs

Parameter	Unit	XM1	XM3	XM2	XM4
$N_{\rm H}$	10^{22} cm^{-2}	$0.05^{+0.03}_{-0.02}$	$0.06^{+0.03}_{-0.02}$	0.04 ± 0.01	0.05 ± 0.01
$E_{\rm line}$	keV	0.91 ± 0.02	0.92 ± 0.02	$0.92^{+0.03}_{-0.04}$	$0.95^{+0.02}_{-0.03}$
σ	keV	$0.15^{+0.03}_{-0.02}$	$0.11^{+0.03}_{-0.02}$	$0.14^{+0.04}_{-0.03}$	0.13 ± 0.03
norm	10^{-5}	$5.71^{+2.90}_{-1.54}$	$3.68^{+2.03}_{-0.96}$	$4.12^{+2.44}_{-1.33}$	$3.86^{+1.67}_{-1.03}$
$T_{\rm thin}$	keV	$0.17^{+0.03}_{-0.04}$	$0.18^{+0.02}_{-0.03}$	$0.22^{+0.02}_{-0.03}$	$0.22^{+0.02}_{-0.03}$
norm$_{\rm thin}$		55^{+95}_{-28}	42^{+85}_{-18}	20^{+19}_{-7}	16^{+13}_{-6}
$T_{\rm slim}$	keV	$0.54^{+0.07}_{-0.05}$	$0.58^{+0.12}_{-0.09}$	$0.78^{+0.08}_{-0.07}$	0.84 ± 0.05
norm$_{\rm slim}$		$0.06^{+0.04}_{-0.03}$	$0.03^{+0.06}_{-0.02}$	0.02 ± 0.01	0.02 ± 0.01
χ^2/dof		165/168	150/140	218/206	275/238
F_x	10^{-13} erg cm^{-2} s^{-1}	5.31 ± 0.12	5.26 ± 0.14	9.24 ± 0.18	11.06 ± 0.17
L_x	10^{39} erg s^{-1}	1.44 ± 0.03	1.43 ± 0.04	2.51 ± 0.05	3.0 ± 0.05

Note. The absorbed flux F_x and luminosity L_x is calculated in the 0.3–10.0 keV energy range. The Galactic absorption is fixed to 0.04×10^{22} cm^{-2}. The p value of the `DISKPBB` model is fixed to 0.50, resembling a slim disk. The distance is assumed to be 4.76 Mpc (Vinokurov et al. 2018) to calculate the luminosity.

epochs ($\sim 0.05 \times 10^{22}$ cm^{-2}), and so is the Gaussian line energy (~ 0.9 keV). The low-energy thin-disk component (represented by the `DISKBB` model) also remains in a similar temperature state in all epochs. However, the `DISKPBB` component exhibits a higher temperature in the epochs XM2 and XM4 compared to the epochs XM1 and XM3. The average `DISKPBB` temperature in the XM2 and XM4 epochs is ~ 1.5 times higher than that in the XM1 and XM3 epochs. The best-fit parameters are noted in Table 3, and the residuals from the best-fit model for the MOS1 spectra are shown in the bottom left panel of Figure 3 for each observation. For visual purposes, the Gaussian component is removed from the best-fit model. The prominent hump-like (or Gaussian) structure is evident in the residual plots. In Figure 4 (top panel), the model components are shown that depict the

contribution of each component and their variation in different epochs.

4.2. Time-resolved Spectroscopy

ULX1 has undergone several flaring episodes, as described in Section 3. This motivates us to carry out a comparative study of the source's spectral properties between flaring and nonflaring epochs. This subsection mainly focuses on epochs XM2 and XM4, where flares are prominent. As described earlier, we divide the XM2 and XM4 epochs into three subepochs: preflare, flare, and postflare. Nonflaring intervals are chosen by adding the preflare and postflare intervals because the spectral flux and properties overlap in these regimes. In Figure 3 in the top middle (XM2) and right (XM4)

Table 4
Time-resolved Spectral Parameters of the XM2 and XM4 Epochs Using the Same Best-fit Model as in Table 3

Parameter	Unit	XM2		XM4	
		Flaring	Nonflaring	Flaring	Nonflaring
N_H	10^{22} cm^{-2}	$0.05^{+0.07}_{-0.02}$		0.07 ± 0.02	
E_{line}	keV	$0.90^{+0.03}_{-0.02}$		$0.91^{+0.02}_{-0.04}$	
σ	keV	$0.19^{+0.11}_{-0.08}$	$0.15^{+0.12}_{-0.05}$	$0.21^{+0.02}_{-0.03}$	$0.09^{+0.06}_{-0.03}$
norm	10^{-5}	$7.09^{+10.98}_{-4.65}$	$5.83^{+29.76}_{-2.5}$	$9.63^{+2.87}_{-3.85}$	$4.35^{+5.33}_{-1.41}$
T_{thin}	keV	$0.18^{+0.10}_{-0.09}$	$0.18^{+0.04}_{-0.09}$	$0.15^{+0.07}_{-0.02}$	$0.18^{+0.02}_{-0.05}$
norm$_{thin}$		32^{+3983}_{-27}	41^{+3139}_{-23}	68^{+259}_{-59}	58^{+204}_{-26}
T_{slim}	keV	$0.89^{+0.21}_{-0.08}$	$0.52^{+0.08}_{-0.05}$	$0.80^{+0.02}_{-0.02}$	$0.56^{+0.18}_{-0.11}$
norm$_{slim}$		0.02 ± 0.01	$0.11^{+0.12}_{-0.07}$	0.04 ± 0.01	$0.05^{+0.14}_{-0.04}$
χ^2/dof		349/327		409/344	
F_x	10^{-13} erg cm^{-2} s^{-1}	$12.36^{+0.45}_{-0.42}$	7.87 ± 0.21	12.49 ± 0.21	6.50 ± 0.25
L_x	10^{39} erg s^{-1}	$3.35^{+0.12}_{-0.11}$	2.14 ± 0.06	3.39 ± 0.06	1.76 ± 0.07

Note. The absorbed flux F_x and luminosity L_x is calculated in the 0.3–10.0 keV energy range. The Galactic absorption is fixed to 0.04×10^{22} cm^{-2}. The p value of the DISKPBB model is fixed to 0.50, resembling a slim disk. The distance is assumed to be 4.76 Mpc (Vinokurov et al. 2018) to calculate the luminosity.

panels, we overplot the flaring and nonflaring spectra from MOS1. This figure shows how spectra of flaring and nonflaring states diverge mainly after 1 keV (as in part already shown in the timing analysis). Below 1 keV, the spectra are mostly consistent.

We fit these time-resolved spectra with the same model as we used for the time-averaged analysis because it was adequate to describe both the steady (XM1 and XM3) and the flaring (XM2 and XM4) observations. The fit of nonflaring and flaring spectra of individual observation is done simultaneously, linking absorption and line energy and letting the disk parameters vary freely. We report the best-fit parameter and error estimates in Table 4. Figure 3 in the bottom middle (XM2) and right (XM4) panels shows the residuals from the best-fit model (without the Gaussian component) for the MOS1 spectra. The nonvarying nature of the DISKBB temperature between flaring and nonflaring episodes is similar to the case of time-averaged spectroscopic results reported in Table 3. The best-fit DISKPBB temperatures in flaring episodes are higher than the temperature in the nonflaring episodes of XM2 and XM4 by ∼1.7 and ∼1.4 times, respectively. As expected, the spectral parameters of the nonflaring episodes of XM2 and XM4 are also consistent with the parameters of the XM1 and XM3 epochs, which do not show any flaring events. Especially, the temperatures of the thin and slim disks are similar in all of these cases, which suggests a steady accretion in the system during these steady (XM1 and XM3) epochs and nonflaring episodes of XM2 and XM4. In Figure 4 (bottom panel), the model components for flaring and nonflaring spectra are shown. They show how the spectral components vary due to flaring events, specifically the DISKPBB component.

5. Discussion and Conclusions

A previous study by Earnshaw & Roberts (2017) showed that the spectra from ULX1 exhibit a steep power-law tail and a strong, Gaussian-like feature near ∼0.9 keV, which could be explained by a mekal model. However, multiple studies suggest that a two-component disks might be more appropriate to describe the spectra of ULXs (Pinto et al. 2017, 2020; Kara et al. 2020; Walton et al. 2020).

It is widely believed that disks around ULXs have a two-tiered structure: very far from the ULX, the disk is a typical

Shakura & Sunyaev (1973)-like thin disk. When the local luminosity of the disk approaches the Eddington limit, the disk inflates, winds are launched that carry away excess mass, and advection plays a central role. In this physical scenario, the low-energy thin-disk component corresponds to the outer disk, and the high-energy slim-disk component corresponds to the emission from the inner disk and the winds. By setting this physical accretion picture, we discuss how these new XMM-Newton observations conform with these scenarios.

The XMM-Newton observations of NGC 4395 ULX1 before 2018 do not show significant short-term variability in the source (Earnshaw & Roberts 2017). The latest 2018–2019 observations, however, show significant flaring episodes in the data. We compare the ULX1 spectral properties with known ULX categories. The hard spectra generated from the radial advection of the slim accretion disk modeled by a DISKPBB component implies the supercritical accretion scenario. The luminosity measurement ($L \sim 1.4$–3.0×10^{39} erg s^{-1}) shows that ULX1 is accreting at or just above the Eddington accretion rate limit if it hosts a typical ∼10 $M_\odot$ black hole. Thus, one might initially expect ULX1 to exhibit a broadened disk spectrum. However, it is crucial to note that the temperature of the hot slim-disk component is lower than the typical temperature of BD ULXs. Moreover, ULX1 spectra require a cool disk component, which is unusual for BD ULXs. Alternatively, one might compare ULX1 with SULs and ULSs judging from the soft nature of the source. In all observations, the source exhibits a power-law photon index of $\Gamma > 2$ in the 0.3–5.0 keV band, hence an apparent classification would be an SUL. However, it is important to consider that many SUL sources (Sutton et al. 2013) show a higher luminosity than the luminosity range of NGC 4395 ULX1. While comparing with ULSs, we observe that the two-disk component spectra in ULX1 are quite distinctive in nature from the single ultrasoft blackbody spectra of ULSs. Thus, we suggest that NGC 4395 ULX1 is a case that is intermediate between SUL and ULS states. The spectral properties of NGC 4395 ULX1, like the spectral profile, the two thermal component continuum, and atomic emission features are similar to those of NGC 55 ULX and NGC 247 ULX-1, in particular (Pinto et al. 2017, 2021). One possible explanation for the soft nature of the source is a geometrical picture when the line of sight is nearer to the plane of the disk, thus obstructing the hard photons coming from the
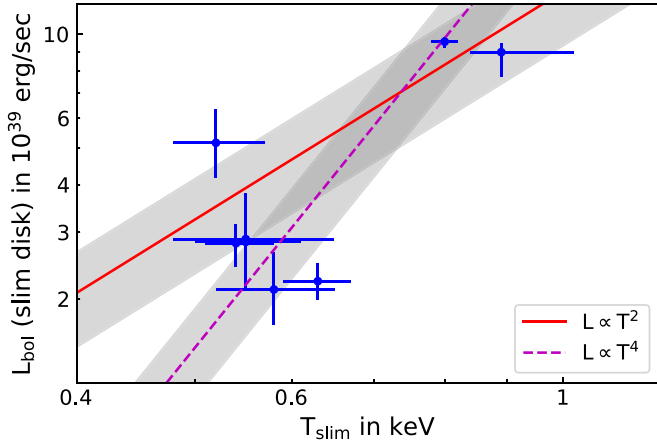
Figure 5. Relation of the unabsorbed bolometric luminosity of the hard slim-disk component vs. temperature of that disk. The shaded regions show the 95% confidence intervals on the normalizations of the power-law relations.

inner and hotter region of the accretion disk (see a similar discussion for NGC 55 ULX in Pinto et al. 2017).

The power spectrum analysis of the time series shows low-frequency red noise explained by a power-law type PSD in a few observations. This often occurs in X-ray binaries due to the variation in mass accretion rate (Uttley & McHardy 2001). We do not find any quasiperiodic or periodic oscillation in addition to the red and white noise in the power spectrum. The soft and hard energy time series in the XM2 and XM4 epochs confirm that the harder spectral components dominate the flaring activity. A comparable behavior in other ULXs (e.g., Middleton et al. 2015a; Gúrpide et al. 2021a, 2021b) can be interpreted as the partial occultation of the inner region of the disk from the wind launched by the super-Eddington disk. This might in principle be the explanation for our results. Another possibility is that we are witnessing a genuine change in accretion rate, leading to the flaring behavior.

An advection-dominated disk, in the absence of beaming, is expected to show a $L \propto T^2$ relation (Kubota & Makishima 2004). This might very well be the case in our data, as shown in Figure 5, where we plot the unabsorbed bolometric luminosity (0.01–10.0 keV) from DISKPBB component and the corresponding disk temperature. To obtain the bolometric DISKPBB flux ($F_{\rm bol}$), we have extended the energies of the instrumental responses in XSPEC following a similar study by Urquhart & Soria (2016). To increase the statistics for the luminosity versus temperature plot, we have also included two additional XMM-Newton observations (ID—0142830101,0200340101), which had comparable exposures to that of the four observations studied here (see the Appendix for the spectral analysis results of these two observations). During these two observations, the source exhibits spectral properties similar to those of the nonflaring epochs of the new observations when fitted with same spectral model. We obtain the bolometric luminosity and disk temperature and their 1σ errors from all observations and fit the data (using scipy.odr routine;[5] Boggs & Rogers 1990) with a $L \propto T^2$ and a $L \propto T^4$ relation. In pursuance of adopting a conservative approach, we consider the larger error on both axes to fit the data points. Figure 5 shows that the luminosity–temperature plane of the DISKPBB model is broadly consistent with the $L \propto T^2$ and

---

$L \propto T^4$ curves. The shaded regions in the figure show the 95% confidence intervals on the normalizations of the power-law relations.

Typically, the bolometric luminosity would be $L_{\rm bol} = \frac{2\pi D^2}{\cos\theta}F_{\rm bol}$, where θ is the disk inclination and D is the distance to the source. A standard assumption is that the disk inclination of these sources is $\sim 60°$ (see Urquhart & Soria 2016 for details), hence $L_{\rm bol} = 4\pi D^2 F_{\rm bol}$, which has been used while estimating the luminosity. Since the inclination angle of the accretion disk is highly uncertain, the absolute value of bolometric luminosity should be taken with caution. However, for a fixed inclination in all epochs, the luminosity–temperature plane would exhibit a fixed positive power-law relation. It is important to note that although the data broadly follow the two curves, empirically, the $L \propto T^2$ relation is more appropriate for an advection-dominated accretion (or slim) disk.

The accretion rate of a slim disk in the presence of advection relates to the luminosity as $L \sim L_{\rm edd}[1 + \ln\dot{m}]$, where $\dot{m}$ is the Eddington factor, the ratio of the accretion rate to the Eddington accretion rate (Shakura & Sunyaev 1973). The ratio of the luminosity during flares to the non-flare periods ($\frac{L_{\rm flare}}{L_{\rm non-flare}} \sim 2$) can then be used to estimate the change in mass accretion rate. Simple algebra leads to the relation of the corresponding Eddington factors of $\dot{m}_{\rm flare} \simeq e \cdot \dot{m}_{\rm non-flare}^2$.

Some authors propose that the apparent change in luminosity in super-Eddington disks might be dominated by the geometrical beaming from the disk winds. In this case, $L \propto L_{\rm edd}[1 + \ln\dot{m}]\dot{m}^2$, because the beaming factor has been proposed to scale as $73/\dot{m}^2$ (King 2009; King & Lasota 2016; King et al. 2017). Since the luminosity ratio in this case is low (~ 2), the luminosity–accretion rate relation can be approximated to $\frac{L_{\rm flare}}{L_{\rm non-flare}} \sim \frac{\dot{m}_{\rm flare}^2}{\dot{m}_{\rm non-flare}^2}$. In that scenario, the Eddington factors corresponding to flaring and nonflaring episodes follow the simple form of $\dot{m}_{\rm flare} \simeq \sqrt{2}\dot{m}_{\rm non-flare}$.

The accretion disk normalizations provide an estimate for the inner radius $R_{\rm in} \simeq \xi\kappa^2 N^{\frac{1}{2}}d_{10}(\cos\theta)^{-\frac{1}{2}}$ km, where ξ is the geometric correction factor and κ is the color-correction factor, d_{10} is the distance in 10 kpc unit, N is the normalization, and θ is the inclination angle of the disk (Kubota et al. 1998; Soria et al. 2015). We estimate the inner radius from the disk normalizations for all the four epochs XM1, XM2, XM3, and XM4. We understand that due to the large uncertainty in the DISKBB normalization measurement in different epochs, the thin accretion disk radius can have a large range of values between $\sim 2000(\cos\theta)^{-\frac{1}{2}}$ and $\sim 7000(\cos\theta)^{-\frac{1}{2}}$ km assuming $\xi \sim 0.412$ and $\kappa \sim 1.7$ (Shimura & Takahara 1995; Kubota et al. 1998). The DISKPBB slim accretion disk normalizations are similar in different epochs, however, hence the inner radius is found by taking a simple average of the DISKPBB normalization from all the four epochs. We would caution that to estimate this inner radius from the DISKPBB model, we assume that the radius is constant, which is appropriate for the $L \propto T^4$ relation. However, from the $L \propto T^2$ relation, the inner radius need not necessarily be constant unless advection plays a significant role. It should also be noted that an estimate of the radius from the DISKPBB model is an approximation of the advection-dominated disk because the DISKPBB is an approximate power-law-scaled model of the radial dependent temperature and does not formally include the physical effects of advection on the inferred inner radius.

Under the assumption of $\xi \sim 0.353$ and $\kappa \sim 3$ for a slim disk (Vierdayanti et al. 2008; Soria et al. 2015), the radius turns out to be $\sim 273 \, (\cos\theta)^{-\frac{1}{2}}$ km. This would correspond to the last stable orbit ($R_{\mathrm{ISCO}} = 6GM/c^2$) of a $\sim 31 \, M_\odot$ nonrotating black hole assuming a face-on disk or a $\sim 43 \, M_\odot$ nonrotating black hole if the disk inclination is $\sim 60^\circ$. On the other hand, this radius would correspond to the magnetospheric radius ($R_M = 7 \times 10^7 \Lambda m^{\frac{1}{7}} R_6^{\frac{10}{7}} B_{12}^{\frac{4}{7}} L_{39}^{\frac{-2}{7}}$ cm; parameters are explained in Mushtukov et al. 2017) of a magnetized neutron star of 1.4 $M_\odot$ with a magnetic field of $\sim 6.1 \times 10^{11}$ Gauss for a face-on disk geometry or $\sim 1.58 \times 10^{12}$ Gauss for a disk inclination of $\sim 60^\circ$. We have used the typical values of $\Lambda \sim 0.5$, a neutron star radius of $\sim 10^6$ cm, and the average luminosity (in 0.3–10.0 keV) measured for the four epochs $\sim 2.1 \times 10^{39}$ erg s^{-1} for the disk inclination of $\sim 60^\circ$ or two times lower for the face-on disk.

If the above interpretations are true, the inner disk component dominates the variable part of the spectrum. This might be due either to an intrinsic change in accretion rate or to a variable clumpy wind that partially occults the inner region and imprints this variability on the hard emission. However, the measured neutral absorption column density does not change during these observations. This suggests that if the wind clouds that block the hotter portions of the disk are not highly ionized, these transient flaring phenomena are related to the inner disk region that lies at a far distance from the wind cloud regions. However, if these regions of wind clouds are highly ionized, changes in line-of-sight scattering would imprint a variability like this.

Another plausible inference regarding the hard photons that are observed during flares could be related to the inverse-Compton scattering process. Due to flaring events, the number of inner disk photons can proliferate owing to the high accretion rate. These photons can further interact with highly energetic electrons via the inverse-Compton process and release harder photons from the coronal region. This produces spectrally harder flaring events compared to nonflaring events.

NGC 4395 ULX1 shows a clear broad emission feature around ~ 0.9 keV. A similar feature has been reported in several other ULXs, such as NGC 1313 X1, NGC 55 ULX, NGC 247 ULX-1 (Pinto et al. 2017, 2020, 2021). This broad ~ 0.9 keV line feature is in reality a combination of multiple emission lines that cannot be resolved by the EPIC instruments. These lines are typically associated with Mg XII, Fe XXII- XXIII, Ne X, Ne IX, O VIII, and O VII lines, as also observed in soft ULXs such as NGC 55 ULX or NGC 247 ULX-1 (see, e.g., Pinto et al. 2017; Kosec et al. 2021). In fact, the broad feature around ~ 1 keV in EPIC data can be modeled by emission lines around ~ 0.9 keV or absorptions around ~ 0.7 and ~ 1.2 keV (Middleton et al. 2014, 2015a). In case of EPIC+RGS combined data, one can fit all emission and absorption features to explain the broad feature (see Pinto et al. 2021). However, with low spectral resolution EPIC-only data, it is a custom to either fit a Gaussian emission or two absorptions (GABS; see Middleton et al. 2015a for details). Due to the well-constrained parameters and simpler nature of the GAUSS model fit in our data, we use this model to explain the broad hump-like feature. However, we cannot discard the presence of absorption lines in ULX1 spectra within the limited spectral resolution of EPIC data. The S/N in RGS data is poor for ULX1 in all four observations, as the background mostly dominates the whole RGS spectra, hence, we were unable to use RGS data to

quantify any emission or absorption feature present in the source. Future X-ray monitoring of the source will be crucial in establishing its transient nature and in better understanding the physical properties.

Appendix
Analysis Results of XMM-Newton Observations (ID-0142830101 and 0200340101)

We discuss the spectral analysis results of ULX1 for the observations 0142830101 (date: 2003-11-30) and 0200340101 (date: 2004-06-02). The data reduction process followed for these two observations is similar to that described in Section 2. In both observations, the source exhibits steep spectra extending only up to 5 keV, similar to the XM1 and XM3 epochs, after which the background starts to dominate. The pn observation of 0142830101 is affected by chip gap and bad column, as happened in the other observations discussed in the

Table A1
Best-fit Model (TBABS(GAL) * TBABS * (GAUSS+DISKBB+DISKPBB)) Parameters of NGC 4395 ULX1 for Observations 0142830101 and 0200340101

Parameter	Unit	0142830101	0200340101
N_{H}	10^{22} cm^{-2}	0.06 ± 0.02	$0.12^{+0.08}_{-0.06}$
E_{line}	keV	0.94 ± 0.02	$0.92^{+0.04}_{-0.06}$
σ	keV	0.09 ± 0.02	0.13 ± 0.03
norm	10^{-5}	$2.37^{+0.71}_{-0.50}$	$6.11^{+5.75}_{-2.47}$
T_{thin}	keV	0.18 ± 0.02	$0.13^{+0.05}_{-0.04}$
norm$_{\mathrm{thin}}$		27^{+35}_{-13}	216^{+2573}_{-184}
T_{slim}	keV	$0.63^{+0.08}_{-0.06}$	$0.55^{+0.11}_{-0.08}$
norm$_{\mathrm{slim}}$		$0.02^{+0.02}_{-0.01}$	$0.05^{+0.06}_{-0.03}$
χ^2/dof		158/155	94/75
F_x	10^{-13} erg cm^{-2} s^{-1}	$4.07^{+0.11}_{-0.10}$	4.19 ± 0.21
L_x	10^{39} erg s^{-1}	1.10 ± 0.03	1.14 ± 0.06

Note. The absorbed flux F_x and luminosity L_x is calculated in the 0.3–10.0 keV energy range. The Galactic absorption is fixed to 0.04×10^{22} cm^{-2}. The *p* value of the DISKPBB model is fixed to 0.50, resembling a slim disk. The distance is assumed to be 4.76 Mpc (Vinokurov et al. 2018) to calculate the luminosity.

paper. We have given a similar treatment as discussed in Sections 2 and 4 to verify the effect of the chip gap and bad column on the source spectral properties in this observation. We simultaneously fit pn and MOS1/2 data by keeping the cross-calibration constant fixed to 1 for MOS1 and by leaving it free to vary for MOS2 and pn. In observation 0200340101, the source is highly off-axis (see also Earnshaw & Roberts 2017) and falls out of the pn detector field of view. Only MOS1 and MOS2 data are used for this observation. The cleaned exposures of pn/MOS1/MOS2 for the 0142830101 observation are 69/93/94 ks. For the 0200340101 observation, the MOS1/MOS2 cleaned exposures are 65/65 ks. The spectral analysis results with the model `TBABS(GAL)*TBABS*(GAUSS+DISKBB+DISKPBB)` are tabulated in Table A1.

ORCID iDs

Tanuman Ghosh ⦿ https://orcid.org/0000-0002-3033-5843
Vikram Rana ⦿ https://orcid.org/0000-0003-1703-8796
Matteo Bachetti ⦿ https://orcid.org/0000-0002-4576-9337

References

Abramowicz, M. A., Czerny, B., Lasota, J. P., & Szuszkiewicz, E. 1988, ApJ, 332, 646
Abramowicz, M. A., Kato, S., & Matsumoto, R. 1989, PASJ, 41, 1215
Andersen, B. C., & Ransom, S. M. 2018, ApJL, 863, L13
Arnaud, K. A. 1996, in ASP Conf. Ser. 101, Astronomical Data Analysis Software and Systems V, ed. G. H. Jacoby & J. Barnes (San Francisco, CA: ASP), 17
Bachetti, M. 2018, HENDRICS: High ENergy Data Reduction Interface from the Command Shell, Astrophysics Source Code Library, ascl:1805.019
Bachetti, M., Harrison, F. A., Walton, D. J., et al. 2014, Natur, 514, 202
Bachetti, M., Rana, V., Walton, D. J., et al. 2013, ApJ, 778, 163
Barnard, R. 2010, MNRAS, 404, 42
Begelman, M. C. 1979, MNRAS, 187, 237
Blackburn, J. K. 1995, in ASP Conf. Ser. 77, Astronomical Data Analysis Software and Systems IV, ed. R. A. Shaw, H. E. Payne, & J. J. E. Hayes (San Francisco, CA: ASP), 367
Blackburn, J. K., Shaw, R. A., Payne, H. E., Hayes, J. J. E., & Heasarc 1999, FTOOLS: A general package of software to manipulate FITS files, Astrophysics Source Code Library, ascl:9912.002
Boggs, P. T., & Rogers, J. E. 1990, Contemp. Math., 112, 183
Brightman, M., Harrison, F. A., Barret, D., et al. 2016, ApJ, 829, 28
Brightman, M., Harrison, F. A., Fürst, F., et al. 2018, NatAs, 2, 312
Carpano, S., Haberl, F., Maitra, C., & Vasilopoulos, G. 2018, MNRAS, 476, L45
Chandra, A. D., Roy, J., Agrawal, P. C., & Choudhury, M. 2020, MNRAS, 495, 2664
Earnshaw, H. M., & Roberts, T. P. 2017, MNRAS, 467, 2690
Earnshaw, H. P., Grefenstette, B. W., Brightman, M., et al. 2019, ApJ, 881, 38
Edelson, R., Turner, T. J., Pounds, K., et al. 2002, ApJ, 568, 610
Fürst, F., Walton, D. J., Harrison, F. A., et al. 2016, ApJL, 831, L14
Fürst, F., Walton, D. J., Stern, D., et al. 2017, ApJ, 834, 77
Gabriel, C., Denby, M., Fyfe, D. J., et al. 2004, in ASP Conf. Ser. 314, Astronomical Data Analysis Software and Systems (ADASS) XIII, ed. F. Ochsenbein, M. G. Allen, & D. Egret (San Francisco, CA: ASP), 759
Gúrpide, A., Godet, O., Koliopanos, F., Webb, N., & Olive, J. F. 2021a, A&A, 649, A104
Gúrpide, A., Godet, O., Vasilopoulos, G., Webb, N. A., & Olive, J. F. 2021b, A&A, 654, A10

HI4PI Collaboration, Ben Bekhti, N., Flöer, L., et al. 2016, A&A, 594, A116
Huppenkothen, D., Bachetti, M., Stevens, A. L., et al. 2019, ApJ, 881, 39
Israel, G. L., Belfiore, A., Stella, L., et al. 2017a, Sci, 355, 817
Israel, G. L., Papitto, A., Esposito, P., et al. 2017b, MNRAS, 466, L48
Jansen, F., Lumb, D., Altieri, B., et al. 2001, A&A, 365, L1
Kaaret, P., & Feng, H. 2009, ApJ, 702, 1679
Kaaret, P., Feng, H., & Roberts, T. P. 2017, ARA&A, 55, 303
Kara, E., Pinto, C., Walton, D. J., et al. 2020, MNRAS, 491, 5172
King, A., & Lasota, J.-P. 2016, MNRAS, 458, L10
King, A., Lasota, J.-P., & Kluźniak, W. 2017, MNRAS, 468, L59
King, A. R. 2009, MNRAS, 393, L41
Kosec, P., Pinto, C., Fabian, A. C., & Walton, D. J. 2018a, MNRAS, 473, 5680
Kosec, P., Pinto, C., Reynolds, C. S., et al. 2021, MNRAS, 508, 3569
Kosec, P., Pinto, C., Walton, D. J., et al. 2018b, MNRAS, 479, 3978
Kubota, A., & Makishima, K. 2004, ApJ, 601, 428
Kubota, A., Tanaka, Y., Makishima, K., et al. 1998, PASJ, 50, 667
Liu, J.-F., & Bregman, J. N. 2005, ApJS, 157, 59
Middleton, M. J., Heil, L., Pintore, F., Walton, D. J., & Roberts, T. P. 2015a, MNRAS, 447, 3243
Middleton, M. J., Walton, D. J., Fabian, A., et al. 2015b, MNRAS, 454, 3134
Middleton, M. J., Walton, D. J., Roberts, T. P., & Heil, L. 2014, MNRAS, 438, L51
Motta, S. E., Marelli, M., Pintore, F., et al. 2020, ApJ, 898, 174
Mukherjee, E. S., Walton, D. J., Bachetti, M., et al. 2015, ApJ, 808, 64
Mushtukov, A. A., Suleimanov, V. F., Tsygankov, S. S., & Ingram, A. 2017, MNRAS, 467, 1202
NASA High Energy Astrophysics Science Archive Research Center (HEASARC) 2014, HEAsoft: Unified Release of FTOOLS and XANADU, Astrophysics Source Code Library, ascl:1408.004
Pinto, C., Alston, W., Soria, R., et al. 2017, MNRAS, 468, 2865
Pinto, C., Middleton, M. J., & Fabian, A. C. 2016, Natur, 533, 64
Pinto, C., Soria, R., Walton, D., et al. 2021, MNRAS, 505, 5058
Pinto, C., Walton, D. J., Kara, E., et al. 2020, MNRAS, 492, 4646
Pintore, F., Marelli, M., Salvaterra, R., et al. 2020, ApJ, 890, 166
Pintore, F., Motta, S., Pinto, C., et al. 2021, MNRAS, 504, 551
Poutanen, J., Lipunova, G., Fabrika, S., Butkevich, A. G., & Abolmasov, P. 2007, MNRAS, 377, 1187
Rana, V., Harrison, F. A., Bachetti, M., et al. 2015, ApJ, 799, 121
Ransom, S. 2011, PRESTO: PulsaR Exploration and Search TOolkit, Astrophysics Source Code Library, ascl:1107.017
Remillard, R. A., & McClintock, J. E. 2006, ARA&A, 44, 49
Rodríguez Castillo, G. A., Israel, G. L., Belfiore, A., et al. 2020, ApJ, 895, 60
Sathyaprakash, R., Roberts, T. P., Walton, D. J., et al. 2019, MNRAS, 488, L35
Shakura, N. I., & Sunyaev, R. A. 1973, A&A, 24, 337
Shimura, T., & Takahara, F. 1995, ApJ, 445, 780
Soria, R., Kuntz, K. D., Long, K. S., et al. 2015, ApJ, 799, 140
Sutton, A. D., Roberts, T. P., & Middleton, M. J. 2013, MNRAS, 435, 1758
Urquhart, R., & Soria, R. 2016, MNRAS, 456, 1859
Uttley, P., & McHardy, I. M. 2001, MNRAS, 323, L26
Vasilopoulos, G., Ray, P. S., Gendreau, K. C., et al. 2020, MNRAS, 494, 5350
Vaughan, S., Edelson, R., Warwick, R. S., & Uttley, P. 2003, MNRAS, 345, 1271
Verner, D. A., Ferland, G. J., Korista, K. T., & Yakovlev, D. G. 1996, ApJ, 465, 487
Vierdayanti, K., Watarai, K.-Y., & Mineshige, S. 2008, PASJ, 60, 653
Vinokurov, A., Fabrika, S., & Atapin, K. 2018, ApJ, 854, 176
Walton, D. J., Fuerst, F., Harrison, F., et al. 2013, ApJ, 779, 148
Walton, D. J., Harrison, F. A., Bachetti, M., et al. 2015a, ApJ, 799, 122
Walton, D. J., Harrison, F. A., Grefenstette, B. W., et al. 2014, ApJ, 793, 21
Walton, D. J., Middleton, M. J., Pinto, C., et al. 2016, ApJL, 826, L26
Walton, D. J., Middleton, M. J., Rana, V., et al. 2015b, ApJ, 806, 65
Walton, D. J., Pinto, C., Nowak, M., et al. 2020, MNRAS, 494, 6012
Wilms, J., Allen, A., & McCray, R. 2000, ApJ, 542, 914
Wilson-Hodge, C. A., Malacaria, C., Jenke, P. A., et al. 2018, ApJ, 863, 9